

Simulation of Adsorption Processes at Metallic Interfaces: An Image Charge Augmented QM/MM Approach

Dorothea Golze,^{*,†} Marcella Iannuzzi,^{*,†} Manh-Thuong Nguyen,[‡] Daniele Passerone,[§] and Jürg Hutter^{*,†}

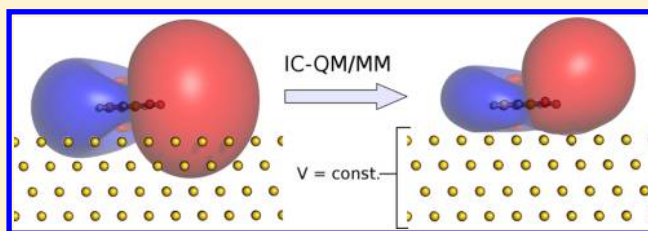
[†]Institute of Physical Chemistry, University of Zürich, Winterthurerstrasse 190, CH-8057 Zürich, Switzerland

[‡]The Abdus Salam International Centre for Theoretical Physics, Strada Costiera 11, I-34151 Trieste, Italy

[§]Empa, Swiss Federal Laboratories for Materials Science and Technology, nanotech@surfaces Laboratory, Überlandstrasse 129, CH-8600 Dübendorf, Switzerland

S Supporting Information

ABSTRACT: A novel method for including polarization effects within hybrid quantum mechanics/molecular mechanics (QM/MM) simulations of adsorbate-metal systems is presented. The interactions between adsorbate (QM) and metallic substrate (MM) are described at the MM level of theory. Induction effects are additionally accounted for by applying the image charge formulation. The charge distribution induced within the metallic substrate is modeled by a set of Gaussian charges (image charges) centered at the metal atoms. The image charges and the electrostatic response of the QM potential are determined self-consistently by imposing the constant-potential condition within the metal. The implementation is embedded in a highly efficient Gaussian and plane wave framework and is naturally suited for periodic systems. Even though the electronic properties of the metallic substrate are not taken into account explicitly, the augmented QM/MM scheme can reproduce characteristic polarization effects of the adsorbate. The method is assessed through the investigation of structural and electronic properties of benzene, nitrobenzene, thymine, and guanine on Au(111). The study of small water clusters adsorbed on Pt(111) is also reported in order to demonstrate that the approach provides a sizable correction of the MM-based interactions between adsorbate and substrate. Large-scale molecular dynamics (MD) simulations of a water film in contact with a Pt(111) surface show that the method is suitable for simulations of liquid/metal interfaces at reduced computational cost.



1. INTRODUCTION

Interfaces between metallic substrates and molecular adsorbates are present in electrolysis, heterogeneous catalysis, transistors, metal-supported nanodevices, and many other applications. The accurate theoretical description of such interfaces requires large simulation cells consisting of several layers in the metallic substrate and sufficient lateral dimensions. A full quantum mechanical treatment of these systems, for example, by means of density functional theory (DFT) is often not affordable due to computational limitations. Computationally less expensive approaches, such as molecular mechanics (MM), can provide a solution but cannot capture electronic effects. An alternative strategy is the usage of a hybrid scheme combining QM and MM methods.¹ In a QM/MM setup of an adsorbate-metal system, the electronic structure of the adsorbate is of primary importance. Thus, the adsorbate is treated by QM and the metal by classical force fields. Such a model implies that the interactions between adsorbate and substrate are described by an empirical potential. However, with standard force fields, it is not straightforward to reproduce polarization effects explicitly. The polarization of metal and adsorbate is caused by electrostatic screening effects in metallic conductors. The electronic distribution of the metal responds to the electrostatic potential generated by the adsorbate, such that the electrostatic potential within the metal is zero or at least a constant when an

external potential is applied. This response can be modeled in terms of an image charge distribution within the metal.^{2,3} Image charges interact with the charge density of the adsorbate and can affect structural and electronic properties of the adsorbed molecule. Experimental and theoretical studies^{4,5} showed that effects associated to the induced charge distribution drive the self-assembly of organic molecules on metallic substrates. Including polarization is also crucial for modeling electrochemical interfaces at metal electrodes. Wernersson et al. demonstrated that neglecting image charges can lead to highly inaccurate forces on the electrolytes and qualitatively wrong results for certain system parameters.⁶ Image charge interactions are also present between the tip of an atomic force microscope (AFM) and the sample generating significant forces on the tip. Therefore, taking these phenomena into account is also important in the interpretation of AFM images, as discussed in refs 7–9.

Several models for capturing polarization effects at metallic interfaces within MM schemes have been addressed in literature. An approach called discrete classical model (DCM) was introduced by Finnis et al.^{10,11} and used for simulations of isopropanol on Pt(111).¹² The basic idea behind this method is

Received: August 6, 2013

Published: September 24, 2013

to model the polarization of the metal by a set of point charges and dipoles assigned to each metal atom. Another MM-based approach tries to reproduce the polarization of the metal by attaching two opposite charges, which are connected by a spring potential or rigid rod, to each atom in the metallic substrate.^{13,14} Both methods do not account for the fact that the image charges modify the charge distribution of the adsorbate and that this in turn changes the polarization of the metal. Therefore, a variational procedure adjusting the induced charges on-the-fly is required. The Gaussian charge method developed by Siepmann and Sprik¹⁵ treats the image charges as dynamical variables and realizes the mutual modification of induced and adsorbate charges. The Siepmann–Sprik scheme has been successfully applied to water/platinum interfaces^{15–17} as well as ionic liquids at platinum¹⁸ and carbon^{19,20} electrodes within a purely classical frame.

Even though QM/MM frameworks are very popular for simulations of biochemical systems,^{21–25} there are only a few cases where QM/MM models have been applied to metallic substrates.^{26,27} Self-consistent techniques are available for the inclusion of polarization effects in QM/MM simulations of bioorganic molecules,^{28–30} but there is no such method, to our knowledge, available for metallic interfaces. This motivates us to adapt the Siepmann–Sprik approach to a QM/MM scheme.

Here, we present an implementation of the image charge (IC) method within a QM/MM framework, where the QM part is treated at the Kohn–Sham (KS) DFT level within a mixed Gaussian and plane wave³¹ (GPW) formalism. In the next section, the theoretical setup is introduced and the implementation details are described. Efficiency and scalability of our method, which is referred to as IC-QM/MM in the following, are also discussed. Different test systems, such as small aromatic molecules adsorbed on Au(111), are used to assess the new approach. We investigate how the interactions of the DFT charge density with the image charges affect interaction and adsorption energies as well as the electronic structure of the adsorbate. The IC-QM/MM approach is applied to small water clusters on Pt(111) and the accuracy of our approach is evaluated by comparing structural and energetic properties to experimental data and full DFT results. “Full DFT” in this context means, that metal as well as adsorbate are treated at the DFT level. Furthermore, results for a large-scale MD simulation of a liquid water/Pt(111) interface are discussed and related to experimental studies.

2. THEORY AND IMPLEMENTATION

2.1. QM/MM Formulation of the Image Charge Approach: IC-QM/MM. The charge distribution $\rho(\mathbf{r})$ of a molecule approaching the metallic surface generates an electrostatic potential (Hartree potential) $V_H(\mathbf{r})$ that extends beyond the surface into the substrate. $V_H(\mathbf{r})$ induces an electrostatic response of the metallic conductor such that the electrostatic potential within the metal is constant. To model this response, Siepmann and Sprik¹⁵ introduced the induced charge distribution $\rho_m(\mathbf{r})$, which in turn generates the potential $V_m(\mathbf{r})$ screening $V_H(\mathbf{r})$ in the region of the substrate. Siepmann and Sprik proposed to define $\rho_m(\mathbf{r})$ as a linear expansion of Gaussian functions centered at the metal atoms,

$$\begin{aligned}\rho_m(\mathbf{r}) &= \sum_a c_a g_a(\mathbf{r}, \mathbf{R}_a) \\ &= \sum_a q_a \left(\frac{\alpha}{\pi} \right)^{3/2} \exp(-\alpha |\mathbf{r} - \mathbf{R}_a|^2)\end{aligned}\quad (1)$$

where \mathbf{R}_a is the position of metal atom a and g_a is the spherical Gaussian function located at a . The width of all Gaussian functions is determined by one single, fixed parameter α , and q_a can be interpreted as magnitude of the induced charge at each position a . The expansion coefficients c_a are unknown and are obtained by imposing the condition that the electrostatic potential is constant for each point \mathbf{r} within the metallic slab,

$$V_H(\mathbf{r}) + V_m(\mathbf{r}) = \int \frac{\rho(\mathbf{r}') + \rho_m(\mathbf{r}')}{|\mathbf{r}' - \mathbf{r}|} d\mathbf{r}' = V_0 \quad (2)$$

In this expression, V_0 is a constant potential that can be different from zero, if an external potential is applied. While in the original Siepmann–Sprik method $\rho(\mathbf{r})$ is obtained from the distribution of point charges associated with the force field, in IC-QM/MM $\rho(\mathbf{r})$ is the KS density plus the charge density assigned to the atomic cores,

$$\rho(\mathbf{r}) = \sum_{\mu\nu} P_{\mu\nu} \chi_\mu(\mathbf{r}) \chi_\nu(\mathbf{r}) + \rho_{\text{core}}(\mathbf{r}) \quad (3)$$

$P_{\mu\nu}$ is the density matrix and $\{\chi_\mu\}$ represents the basis of contracted Gaussian functions used to expand the molecular orbitals.

The electrostatic energy E_{el} is given by

$$\begin{aligned}E_{\text{el}} &= \frac{1}{2} \iint \frac{(\rho(\mathbf{r}) + \rho_m(\mathbf{r}))(\rho(\mathbf{r}') + \rho_m(\mathbf{r}'))}{|\mathbf{r}' - \mathbf{r}|} d\mathbf{r} d\mathbf{r}' \\ &\quad - \int V_0 \rho_m(\mathbf{r}) d\mathbf{r}\end{aligned}\quad (4)$$

Instead of imposing the condition of eq 2, this constraint is modified such that only the weighted integral of eq 2 is forced to a constant. This is equivalent to requiring that the gradients of E_{el} with respect to the coefficients c_a are zero; that is, E_{el} has to be minimized as function of the variables c_a . Thereby, the following set of linear equations is obtained,

$$\begin{aligned}\frac{\partial E_{\text{el}}}{\partial c_a} &= 0 \\ &= \int (V_H(\mathbf{r}) + V_m(\mathbf{r}) - V_0) \cdot g_a(\mathbf{r}) d\mathbf{r} \\ &= \int (V_H(\mathbf{r}) - V_0) g_a(\mathbf{r}) d\mathbf{r} \\ &\quad + \sum_b c_b \iint \frac{g_b(\mathbf{r}') \cdot g_a(\mathbf{r})}{|\mathbf{r}' - \mathbf{r}|} d\mathbf{r} d\mathbf{r}' \\ &= \int (V_H(\mathbf{r}) - V_0) g_a(\mathbf{r}) d\mathbf{r} + \sum_b c_b T_{ab}\end{aligned}\quad (5)$$

Here, T_{ab} are the Coulomb integrals between two spherical Gaussian functions centered at two different metallic centers. These integrals are stored in an $N_{\text{IC}} \times N_{\text{IC}}$ matrix, where N_{IC} is the number of metal centers carrying an image charge. Solving the linear set of equations yields the unknowns c_a and the potential $V_m(\mathbf{r})$ can be calculated. This potential is then added to $V_H(\mathbf{r})$ and the corrected electrostatic term is added to the

Hamiltonian. New molecular orbitals and a new KS charge density are obtained by solving the KS equations for the corrected Hamiltonian. As usual in DFT calculations, this procedure is iterated until self-consistent convergence of the electronic structure optimization is achieved. Thanks to the self-consistent optimization scheme, the polarization of the QM subsystem induced by the interaction with the metal is automatically taken into account.

It can be easily demonstrated that our QM/MM formulation of the IC method provides the correct solution for E_{el} . The electrostatic energy of a charge distribution in the vicinity of a metal is equivalent to the Coulomb energy between the real charges and half of the Coulomb interaction energy between real charges and image charges.² Assuming for simplicity that $V_0 = 0$, the electrostatic energy given in eq 4 has to be consequently equivalent to

$$E_{\text{el}} = \frac{1}{2} \iint \frac{\rho(\mathbf{r}) \cdot \rho(\mathbf{r}')}{|\mathbf{r}' - \mathbf{r}|} d\mathbf{r} d\mathbf{r}' + \frac{1}{2} \iint \frac{\rho(\mathbf{r}) \cdot \rho_{\text{m}}(\mathbf{r}')}{|\mathbf{r}' - \mathbf{r}|} d\mathbf{r} d\mathbf{r}' \quad (6)$$

Employing the condition given by eq 5 (second line), it can be shown that the other two terms indeed vanish,

$$\frac{1}{2} \iint \rho_{\text{m}}(\mathbf{r}) \frac{\rho(\mathbf{r}') + \rho_{\text{m}}(\mathbf{r}')}{|\mathbf{r}' - \mathbf{r}|} d\mathbf{r} d\mathbf{r}' = \frac{1}{2} \sum_a c_a \underbrace{\int g_a(\mathbf{r}) (V_{\text{H}}(\mathbf{r}) + V_{\text{m}}(\mathbf{r})) d\mathbf{r}}_{=0} \quad (7)$$

The IC-QM/MM approach differs from the original Siepmann–Sprik method in several aspects. In the classical version of the IC approach, the potential is rigorously forced to a constant at every metal site \mathbf{R}_a , whereas in IC-QM/MM a condition on the potential is imposed at every real-space grid point \mathbf{r} . The condition we employ is that the integral of the potential weighted by a localized Gaussian function equals zero, see eq 5. This guarantees that the quantity $V_{\text{H}} + V_{\text{m}}$ is approximately constant over the whole space of the metallic slab, which is not the case in the original scheme. Therefore, IC-QM/MM is expected to be numerically more stable with respect to the parameter α as discussed below.

When forces are required, for example, for geometry optimizations or MD runs, the force contributions of the image charges have to be considered. The total gradient of the electrostatic energy with respect to the atomic positions \mathbf{R}_i of the QM atoms is

$$\begin{aligned} \frac{\partial E_{\text{el}}}{\partial \mathbf{R}_i} &= \int \frac{\partial E_{\text{el}}}{\partial \rho(\mathbf{r})} \frac{\partial \rho(\mathbf{r})}{\partial \mathbf{R}_i} d\mathbf{r} \\ &= \sum_{\mu\nu} P_{\mu\nu} \int (V_{\text{H}}(\mathbf{r}) + V_{\text{m}}(\mathbf{r})) \frac{\partial \chi_{\mu}(\mathbf{r}, \mathbf{R}_i) \chi_{\nu}(\mathbf{r}, \mathbf{R}_i)}{\partial \mathbf{R}_i} d\mathbf{r} \end{aligned} \quad (8)$$

The contribution of the image charges to the gradients on the MM atoms (metal) are given by

$$\begin{aligned} \frac{\partial E_{\text{el}}}{\partial \mathbf{R}_a} &= \int \frac{\partial E_{\text{el}}}{\partial \rho_{\text{m}}(\mathbf{r})} \frac{\partial \rho_{\text{m}}(\mathbf{r})}{\partial \mathbf{R}_a} d\mathbf{r} \\ &= c_a \int (V_{\text{H}}(\mathbf{r}) + V_{\text{m}}(\mathbf{r})) \frac{\partial g_a(\mathbf{r}, \mathbf{R}_a)}{\partial \mathbf{R}_a} d\mathbf{r} \end{aligned} \quad (9)$$

Since $V_{\text{H}} + V_{\text{m}}$ is only approximately constant within the metal, the integration over \mathbf{r} in the region of the metal will yield very small contributions. The localized Gaussians g_a decay rapidly to

zero resulting in a zero-contribution of these terms for regions outside the metal.

2.2. Implementation Details. The IC method has been implemented in the QM/MM^{32,33} part of the CP2K³⁴ program package. So far, the QM/MM driver of CP2K provided only an efficient scheme for calculating electrostatic interactions between permanently charged MM atoms and QM charge density. Our implementation is based on the GPW approach,^{31,35} which allows to represent the image charge density $\rho_{\text{m}}(\mathbf{r})$ on a regular grid. Within the GPW formalism, this is equivalent to an expansion of the density in an auxiliary basis set of plane waves. The latter allows to solve the Poisson equation in reciprocal space yielding the potential $V_{\text{m}}(\mathbf{G})$, where \mathbf{G} is the reciprocal lattice vector. The potential in real space $V_{\text{m}}(\mathbf{r})$ is obtained by a subsequent inverse Fast Fourier Transform (FFT⁻¹). Periodic boundary conditions (PBC) follow directly from calculating the potential in Fourier space. Note that the QM and MM boxes need to be of the same size, since the KS and IC density have to be represented on commensurate grids. For systems with a small QM region and a very large MM subsystem, this requirement could substantially contribute to the computational cost.

To obtain the density $\rho_{\text{m}}(\mathbf{r})$, the linear set of equations given in eq 5 is solved by employing a Gaussian elimination scheme or a conjugate gradient (CG) procedure. In both cases the integral I_a

$$I_a = \int (V_{\text{H}}(\mathbf{r}) - V_0) g_a(\mathbf{r}) d\mathbf{r} \quad (10)$$

needs to be computed for each IC center a at every iteration of the SCF cycle. When using a Gaussian elimination scheme, the coefficient matrix \mathbf{T} ,

$$T_{ab} = \iint \frac{g_b(\mathbf{r}', \mathbf{R}_b) \cdot g_a(\mathbf{r}, \mathbf{R}_a)}{|\mathbf{r}' - \mathbf{r}|} d\mathbf{r} d\mathbf{r}' = \int v_b(\mathbf{r}) g_a(\mathbf{r}) d\mathbf{r} \quad (11)$$

is calculated following the algorithm illustrated in Figure 1. The potential v_b generated by a single Gaussian charge b is obtained

```

Loop over all b atoms
  Collocate  $g_b(\mathbf{r})$  on the real space grid
  Transfer to reciprocal space:  $g_b(\mathbf{r}) \xrightarrow{\text{FFT}} g_b(\mathbf{G})$ 
  Solve Poisson equation:  $g_b(\mathbf{G}) \rightarrow v_b(\mathbf{G})$ 
  Transfer back to real space:  $v_b(\mathbf{G}) \xrightarrow{\text{FFT}^{-1}} v_b(\mathbf{r})$ 
  Loop over all atoms a with a >= b
    Calculate integral  $\int v_b(\mathbf{r}) g_a(\mathbf{r}) d\mathbf{r}$ 
  End a loop
End b loop

```

Figure 1. Pseudocode for calculating matrix \mathbf{T} . The inner loop iterates solely over all a larger or equal to atom index b because \mathbf{T} is symmetric.

after solving the Poisson equation in reciprocal space. After an inverse FFT step, v_b is transferred to real space and the integrals T_{ab} are computed by numerical integration on the real space grid. In total, $2N_{\text{IC}}$ FFT are performed, while the number of integrals reduces to $(N_{\text{IC}}^2/2 + N_{\text{IC}}/2)$, because \mathbf{T} is symmetric. Since matrix \mathbf{T} does not depend on $\rho(\mathbf{r})$, it needs to be calculated only once at the very beginning of the SCF cycle. However, for large N_{IC} , computing the single Gaussian

potentials v_b on the full grid can become a bottleneck for the performance.

The iterative CG scheme can be used as alternative algorithm to solve the set of linear equations. The expansion coefficients c_a are initially guessed and ρ_m and V_m are calculated. The CG procedure is then applied to update the coefficients iteratively until the electrostatic energy is minimized. At each iteration of the CG, only two FFTs and the calculation of N_{IC} numerical integrals are required, which can, in principle, be computationally more efficient than the exact calculation of matrix T . However, the CG optimization requires several iterations that need to be performed at every SCF step. To ensure a fast convergence of the CG, a proper preconditioning of the gradient is applied. The optimal choice for the preconditioner is a good approximation of the matrix T . In practice, we always compute T in the first step. Geometry optimizations and MD simulations can exploit the fact that the same matrix T can be used as CG preconditioner for several configurations before being updated. Therefore, the Gaussian elimination scheme is always the method of choice for single point calculations. The preconditioned-CG is used for geometry optimizations and MD simulations.

Our implementation is designed to enable simulations of large systems and takes advantage of the massive parallelization procedures already present in the CP2K program package.

3. COMPUTATIONAL DETAILS

3.1. Static Simulations. The IC-QM/MM approach has been tested on five different adsorbate–metal systems involving physi- and chemisorbed molecules. These are benzene, nitrobenzene, thymine, and guanine adsorbed on Au(111) as well as water adsorbed on Pt(111). The DFT optimized structures are displayed in Figure 2. In the case of H₂O/Pt, a

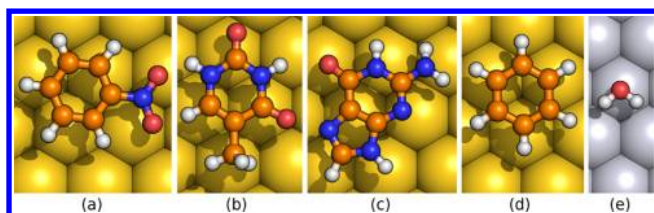


Figure 2. DFT optimized structures of the five investigated molecules adsorbed on a metallic surface: (a) nitrobenzene, (b) thymine, (c) guanine, (d) benzene on Au(111), and (e) water on Pt(111). Color code: orange, C; white, H; blue, N; red, O; yellow, Au; gray, Pt.

water dimer and a cluster of 12 molecules have also been considered. The metallic substrates are modeled by a four-layer slab and PBC are applied in all three dimensions. In order to properly accommodate the adsorbates on the surface, avoiding spurious interactions with the periodic images, $p(12 \times 12)$ replica of the unit cell are used in the lateral dimensions. To decouple the periodic images in the dimension perpendicular to the surface, a vacuum of 25 Å is added along the [111] direction. The slab structure is asymmetric, meaning that the molecule is adsorbed only on one side of the slab, while the atoms of the lowest metal layer are kept fixed in the bulk positions.

Full DFT calculations are performed as reference and compared to QM/MM results obtained with and without IC correction. All calculations are carried out with the CP2K program package.³⁴ For QM calculations, double- ζ valence plus

polarization (DZVP) basis sets of the Molopt-type³⁶ are used to represent the valence electrons. The interactions between valence and core electrons are described by norm-conserving Goedecker, Teter, and Hutter pseudopotentials.^{37–39} The Perdew–Burke–Ernzerhof (PBE) functional⁴⁰ models the exchange and correlation potential. Van der Waals interactions are accounted for by employing Grimme’s D3 dispersion correction.⁴¹ The energy cutoff for the auxiliary plane wave expansion of the density is set to 400 Ry.

At the MM level of theory, Au and Pt are described through embedded atom model (EAM) potentials⁴² obtained from the LAMMPS⁴³ database. Lattice constants were optimized at the respective level of theory. For Au, lattice parameter of 4.08 Å (EAM) and 4.20 Å (DFT) are used, whereas the experimental spacing of 3.92 Å is employed for both, EAM and DFT, in case of Pt. Using the same lattice constants for EAM and DFT is possible for Pt, since the DFT spacing deviates by less than 2% from the experimental (EAM) one.

The MM-based interactions between metal and molecule are modeled with empirical potentials reproducing dispersion, Pauli repulsion and, for H₂O/Pt, specific chemisorption terms. Induction effects are accounted for by image charges. A modified Born–Mayer potential,

$$V(r_{ij}) = A_{ij} \exp(-r_{ij}/\kappa) - C_{ij} r_{ij}^{-6} f_{\text{dmp}}(r_{ij}) \quad (12)$$

is employed for the interactions between Au and adsorbed molecules. The parameters were taken from ref 44. The attractive term was modified with a damping function f_{dmp} as used in ref 45 in order to reproduce the full DFT molecule–surface separation. This potential is not expected to reproduce accurate structures but is only instrumental to estimate the effects of the IC method on a standard QM/MM setup.

Interactions between water molecules and Pt are computed from the Siepmann–Sprik potential,¹⁵ which has been implemented in the MM module of CP2K. The chemisorption potential by Siepmann and Sprik is a sum of two- and three-body terms. It was parametrized to correctly model the ground state geometry and potential curves determined by *ab initio* cluster calculations.

Different structural and electronic properties have been analyzed for the optimized structures. In particular, interaction energies E_{int} are calculated according to

$$E_{\text{int}} = \frac{E_{\text{slab+mol}} - (E_{\text{slab}} + E_{\text{mol}})}{n} \quad (13)$$

where $E_{\text{slab+mol}}$ denotes the total energy of the optimized adsorbate–metal system and n the number of adsorbed molecules. E_{slab} and E_{mol} are the energies of the slab and molecules in the geometry of the complex, respectively. Adsorption energies are instead computed from the energies of the optimized individual components as

$$E_{\text{ads}} = \frac{E_{\text{slab+mol}} - (E_{\text{slab}}^{\text{opt}} + nE_{\text{mol}}^{\text{opt}})}{n} \quad (14)$$

The interaction and adsorption energies obtained from full DFT calculations are affected by the basis set superposition error and have been corrected by the counterpoise formalism.^{46,47}

Electron density differences $\Delta\rho_{\text{elec}}$ are used to investigate changes in the molecular electronic distribution induced by the metal. $\Delta\rho_{\text{elec}}$ is obtained as grid-based difference of $\rho_{\text{elec}}^{\text{slab+mol}}$ and

the electronic densities of the individual components, taken with atomic coordinates as in the complex,

$$\Delta\rho_{\text{elec}} = \rho_{\text{elec}}^{\text{slab+mol}} - \rho_{\text{elec}}^{\text{slab}} - \rho_{\text{elec}}^{\text{mol}} \quad (15)$$

For purpose of representation, we introduce the one-dimensional electron density difference integrated in the planes parallel to the surface,

$$\Delta\rho_{\text{elec}}^{1D} = \int \Delta\rho_{\text{elec}} dx dy \quad (16)$$

Furthermore, molecular dipole moments are computed from the positions of the atomic cores and the centers of maximally localized Wannier orbitals (MLWO).^{48,49}

3.2. MD Simulation. IC-QM/MM has also been applied to perform an MD simulation of the liquid water/Pt(111) interface. The supercell of the substrate is modeled laterally with a $p(6 \times 8)$ repetition of the unit cell and vertically by four metal layers. The Pt(111) surface is surmounted by a 15 Å thick liquid water film, consisting of 151 molecules. Above the water system, 20 Å of vacuum space are introduced to decouple the periodic images along the vertical axis. The QM/MM setup is identical to the setup of the static water/Pt(111) calculations. The simulation is performed within the microcanonical (NVE) ensemble at a temperature of 330 K and a time step of 1 fs is used. The system has been equilibrated for 25 ps employing velocity rescaling for the first 18 ps. The last 55 ps of the simulation have been used for analysis of structural features. The measured drift of the total energy is in the range of 10^{-5} eV/ps/atom during the production run. MLWO were calculated every fifth time step for the last 40 ps of the simulation and used for calculation of the average molecular dipole moments. For analysis of the electronic rearrangement, $\Delta\rho_{\text{elec}}$ has been calculated and averaged for ten equally spaced snapshots.

4. TESTS AND APPLICATIONS

4.1. Gaussian Width α and Performance. The only adjustable variable in the IC-QM/MM scheme is the width α of the Gaussian charge distribution ρ_m , see eq 1. To assess the influence of α on the electrostatic interaction energy, test calculations using the thymine-gold system have been performed. The dependence of total energy and gradients on the Gaussian width is reported in Figure 3. For values of α larger than 3.0 \AA^{-2} , neither the total energy nor the image charge contribution to the gradients show a significant dependency on α . However, drastic changes are found for smaller values. Small values of α correspond to very broad Gaussians, which results in a uniform charge distribution across the metal; that is, the Gaussians are no longer localized at the atomic centers. This leads obviously to nonphysical results arising from technical artifacts. Using extremely large values for α is also not recommendable because very steep Gaussians are not accurately described by a mesh representation over finite grids. For the calculations discussed in the following, a value of 3.0 \AA^{-2} has been chosen.

In order to evaluate the performance of our IC-QM/MM implementation, the average time needed for a single point calculation for thymine on Au(111) has been estimated. The additional computational cost introduced by the IC correction is mainly determined by the evaluation of matrix **T**, given in eq 11. The test system consists of 576 metal atoms resulting in a matrix of size 576×576 . Consequently, FFT has to be

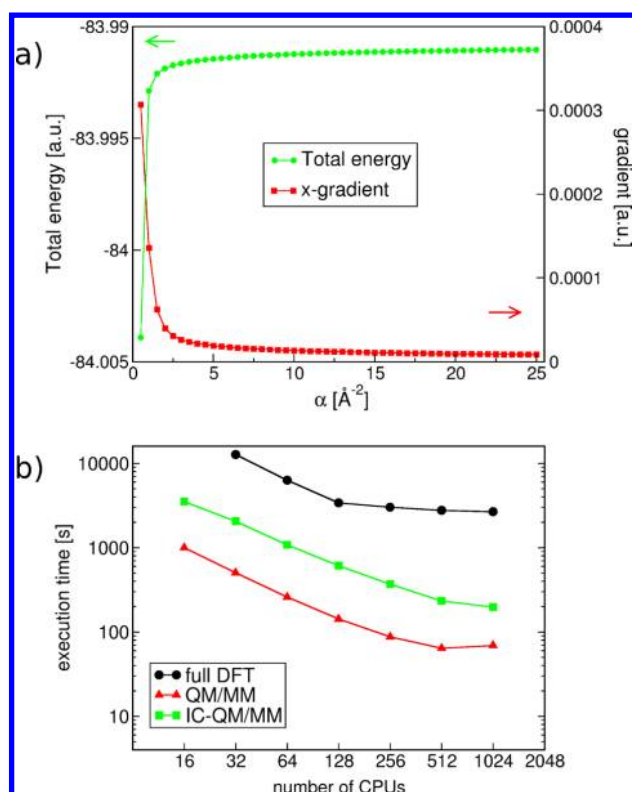


Figure 3. Technical parameters. (a) Dependence of total energy and x-gradients (of an arbitrary metal atom) on parameter α . The x-gradients refer to the IC contribution, see eq 9. (b) Execution time of a single point calculation of thymine on Au(111) performed on a Cray XK6 system. Note that a double logarithmic scale is employed.

performed 1152 times and 166 176 integrals have to be calculated. The parallel efficiency of the IC-QM/MM scheme is shown in Figure 3(b). For this system, the scaling is good up to 1024 cores, while beyond this limit no further speed-up is possible due to load-balancing effects. The comparison of timings reported in Figure 3(b) also shows that by introducing the IC approximation, the QM/MM calculations become four times slower. However, IC-QM/MM is still up to 14 times faster than a full DFT calculation.

4.2. Aromatic Adsorbates on Au(111). **4.2.1. Electrostatic Potential and Induced Charges.** Isosurfaces of the electrostatic potential as obtained by full DFT, IC-QM/MM and QM/MM are displayed for nitrobenzene on Au(111) in Figure 4. The electrostatic potential V_H generated by the adsorbed molecule in the QM/MM calculation extends inside the metallic substrate. By applying the IC correction, the screening of the metal is imposed. As mentioned before, $V_H + V_m$ is not required to be exactly zero but only its weighted

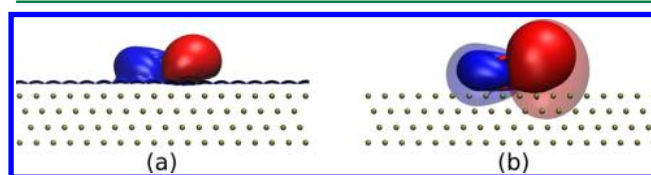


Figure 4. Nitrobenzene on Au(111). Isosurface of the electrostatic potential obtained with (a) full DFT, (b) IC-QM/MM (solid), and (c) QM/MM (transparent). For IC-QM/MM, the electrostatic potential corresponds to $V_m + V_H$ as defined in eq 2. Red: vacuum value + 0.004 a.u. Blue: vacuum value - 0.004 a.u.

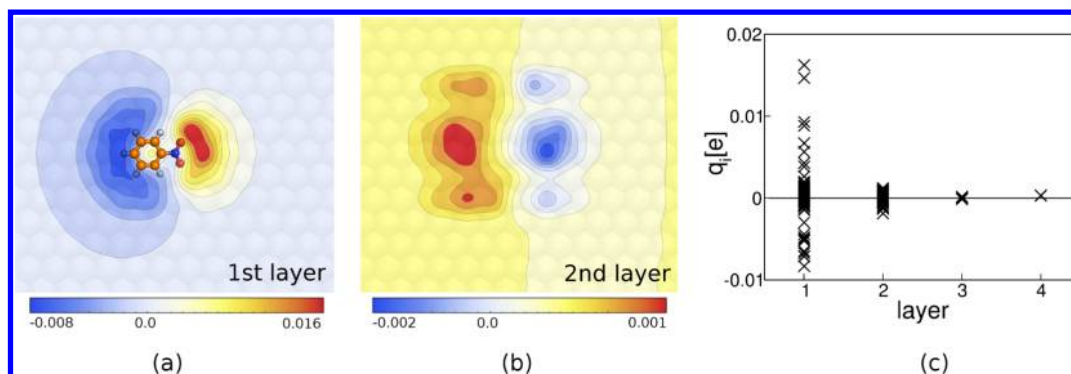


Figure 5. Image charges induced in a 4-layer Au(111) slab by a nitrobenzene molecule. Charge distribution induced in the first (a) and second (b) metal layer. Magnitude q_i of the induced charges in layer 1–4 (c).

integral. However, the sum of $V_H + V_m$ is basically zero at every grid point \mathbf{r} inside the slab, as evident from Figure 4(b) and the contour plots of the potential in Supporting Information (SI) Figure S1. Comparing IC-QM/MM to full DFT, qualitatively similar potentials are obtained. However, the potential in the immediate vicinity (i.e., within the van der Waals radii) of the metallic centers of the first layer is not correctly reproduced by IC-QM/MM. The reason is that IC-QM/MM does not take into account the explicit electronic structure of the substrate neglecting the spatial expansion of the electron shell.

Despite the fact that image charges are introduced to capture a macroscopic effect, investigation of induced charges at an atomistic level reveals some interesting features. The IC distribution induced by nitrobenzene on Au(111) is displayed in the contour plots of Figure 5(a and b). The induction effect occurs mainly in the first layer, while its magnitude decreases rapidly with the distance from the surface. Compared to the first layer, charges induced in the second layer are an order of magnitude smaller. In the third and fourth layer, the induction effect essentially vanishes, see Figure 5(c). It is further observed that, as expected, the electronegative *nitro* group induces positive charges and the electropositive benzene ring induces negative image charges in the first layer. The inverse distribution is found in the second layer.

The total sum of the image charges for the given test system is in the order of 10^{-2} . This sum is expected to converge to zero when reaching the macroscopic continuum limit,^{15,18} that is, in the limit of an infinite metal slab (see also SI Figure S2). However, the finite sum of the image charges does not correspond to a physical charge since the image charges are merely a computational tool to impose the correct behavior of the electrostatic potential.

4.2.2. Geometries and Energetics. For nitrobenzene, thymine and guanine adsorbed on Au(111), full DFT structure optimizations yield basically a planar geometry of the adsorbate with an adsorbate–surface separation $d_{\text{ad-metal}}$ of about 3.1 Å. An almost planar structure has been obtained for benzene/Au(111) with benzene adsorbed at an fcc 3-fold hollow site and $d_{\text{ad-metal}} = 3.0$ Å, which is in agreement with the results reported in ref 50. High symmetry adsorption sites are not observed for nitrobenzene, thymine, and guanine. The optimization of the molecular structures by QM/MM also results in planar geometries and the metal–molecule separations are in agreement with the DFT ones. The QM/MM structures are almost unchanged upon the introduction of image charges, which is attributed to the relatively large molecule–substrate separations. The reason is that the induction effect is relatively weak

and the related force contributions are too small to noticeably change the structure.

The interaction and adsorption energies are computed for thymine and guanine and reported in Table 1. The

Table 1. Interaction E_{int} (kJ/mol) and Adsorption Energies E_{ads} (kJ/mol) of Thymine and Guanine on Au(111)^a

	thymine		guanine	
	E_{int}	E_{ads}	E_{int}	E_{ads}
QM/MM	−59.4	−58.3	−67.0	−65.5
IC-QM/MM	−63.3	−62.3	−73.1	−71.4
$\Delta_{\text{IC-QM/MM}}$	−3.9	−4.0	−6.1	−5.9

^aEnergies are given for the structure optimized with the respective method.

contributions to interaction and adsorption energies arising from polarization lies in the range of -4 to -6 kJ/mol, which coincides with the values given in ref 15. Comparing thymine and guanine, it appears that the polarization energy is larger for the latter. This is attributed to the larger dipole moment (see below) of guanine causing a stronger induction effect. As expected, the IC correction strengthens the interaction between the adsorbate and metal. Nonetheless, energies obtained with full DFT deviate up to -40 kJ/mol from the QM/MM results. Having chosen existing MM interaction pair potentials, not parametrized for the specific model described in this work, we cannot expect a better agreement with the DFT values. Our goal is the assessment of the IC approach. The development of better force fields for these test cases is beyond the scope here.

Even better understanding of the energetic aspects of the interaction with the induced charges is provided by the variation of the molecule–surface separation. In the plots displayed in Figure 6, z is the height of the molecule above the surface, and z_{eq} is the height corresponding to the optimized geometry. Panel (a) of Figure 6 shows the variation of the total QM energy E_{QM} and the image energy E_{IC} of thymine adsorbed on Au(111). E_{IC} is the energy of the molecule derived from the interaction between the molecular charge density and the IC distribution (second term of eq 6). This energy term decreases (in absolute terms) monotonically by increasing the distance. The modulation of E_{QM} is due to the presence of the image charges, which induce a self-consistent perturbation of the electronic structure of the molecule. In plain QM/MM calculations, E_{QM} of the molecule is not affected by the separation from the metal. If the self-consistent treatment

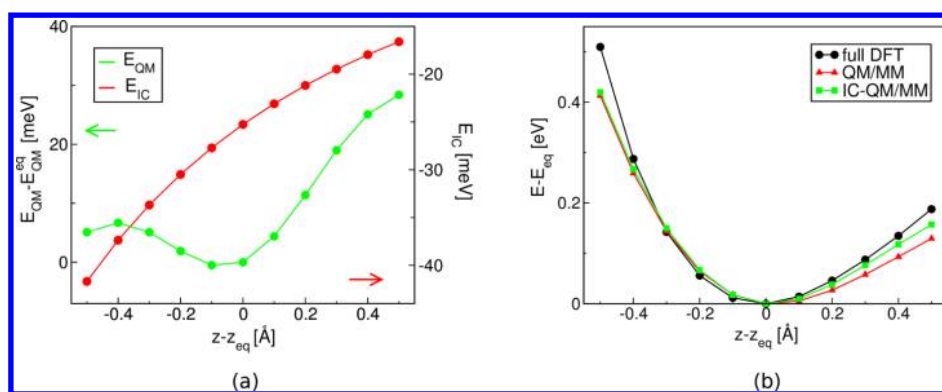


Figure 6. Potential curves. (a) Image energy E_{IC} and difference in total QM energy E_{QM} vs thymine-Au(111) separation for IC-QM/MM. (b) Difference in total energy E vs thymine-Au(111) separation. E_{eq} and E_{QM}^{eq} are the energies at equilibrium distance z_{eq} . The potential curves have been calculated for the structure optimized with the respective method.

would be omitted, E_{QM} would display the same behavior as E_{IC} and a minimum at z_{eq} could not be observed.

The variation of the total energy E vs the distance from the substrate are reported in panel b of Figure 6. For separations larger than the equilibrium distance, the image charges significantly increase the steepness of the QM/MM curve and approximate the full DFT curve better. Including polarization accounts in this case for roughly half of the difference between full DFT and QM/MM. Considering distances between z_{eq} and $z > -0.4$ Å, all three curves coincide. For values smaller than $z = -0.4$ Å, the full DFT curve is steeper indicating repulsive interactions that are not captured by our relatively simple polarization model. Since image charges are modeling a long-range effect, it is reasonable that improvements are obtained for $z > z_{eq}$ but only very limited for $z < z_{eq}$.

4.2.3. Electronic Structure. In the self-consistent procedure, the induced charge density ρ_m and the molecular density ρ mutually modify each other. In order to study the electronic structure rearrangements of the adsorbate, we investigated the difference in electron density $\Delta\rho_{elec}$ upon adsorption of benzene on Au(111). This system is an ideal test candidate, since, due to its planar and highly symmetric structure, polarization is only occurring vertically to the molecule plane. Figure 7(a) shows $\Delta\rho_{elec}$ for benzene as obtained with IC-QM/MM. Accumulation of electron density (red) is observed below and depletion (blue) above the ring plane. The vertical rearrangement of the electron density points at a polarization of the π -electron system toward the surface. This is also clearly appearing in the plots of the plane-integrated density difference $\Delta\rho_{elec}^{1D}$ see Figure 7(b–d). Negative values of $\Delta\rho_{elec}^{1D}$ correspond to depletion and positive values to accumulation of electrons. Figure 7(b) presents $\Delta\rho_{elec}^{1D}$ for benzene located at its equilibrium position z_{eq} as obtained by full DFT. Close to the position of the benzene (red sphere), IC-QM/MM shows the expected negative peak above and a positive peak below the ring plane. However, $\Delta\rho_{elec}^{1D}$ obtained by full DFT is by a factor of 10 larger than predicted by IC-QM/MM and the shape of the peaks is more sophisticated. As obvious from the one- and three-dimensional representations of $\Delta\rho_{elec}$ (see also SI Figure S3(a)), the density between benzene and substrate is not separated. Bader charge analysis^{51,52} implies a charge transfer of 0.14 electrons from benzene toward the surface. The cumulative integral of $\Delta\rho_{elec}$ displayed in SI Figure S3(b), shows the loss of electrons vertically to the surface plane and confirms the value obtained by the Bader charges. From that, we can conclude that the molecule is not solely physisorbed on

the surface but that considerable electronic interactions between benzene and Au(111) occur. This type of interactions at short distances cannot be reproduced by polarization models like the IC approach alone.

By rigidly displacing benzene to larger distances from the metal, the overlap between the surface and molecular states is reduced. At large distances, the only perturbation remaining must be attributed to polarization. As demonstrated by the plots in panels c and d of Figure 7, the agreement between DFT and IC-QM/MM in the region of the adsorbate is also quantitatively very good in this case. By construction, the electronic structure of the metal cannot be reproduced within the IC model.

To further study electronic effects due to polarization, molecular dipoles have been calculated from the position of the Wannier centers as obtained for the structures optimized with the IC-QM/MM method. Without the IC contributions, the electronic structure of the molecule is not affected by the presence of the metal. Therefore, the electronic properties are expected to be those of the molecule in gas phase, apart from small modifications induced by the slight geometrical rearrangement of the physisorbed system. The polarization of the electronic structure through the IC potential is, instead, well recognized in the increased dipole moments of all three tested molecules, see Table 2. The single components of the dipole vectors μ_x , μ_y , and μ_z refer to the molecule and axis orientation displayed in Figure 8. Since the adsorbed molecules are almost planar, the dominant components of the dipoles are those in the xy plane. The largest changes of the dipole due to IC polarization is also observed within this plane. This corresponds to an enhancement of the charge separation within the molecule between the more electronegative and the more electropositive groups. Only in the case of guanine, which already has a positive μ_z component, we observe a non-negligible increment of the dipole also along the z -axis.

QM/MM calculations neglecting induction cannot capture the effect that the dipole moment is sensitive to the molecule-surface separation. Displacing the molecule along the z -axis, the stronger or weaker interaction with the image charges causes a modulation of the molecular dipole. Figure 9 exemplary displays distance-dependent alterations of the lateral component of the dipole moment as well as its magnitude for guanine on Au(111). We observe that the enhancement induced by the image charges decays as the inverse of the distance from the metal, which is indeed the asymptotic long-range behavior of the IC potential. For large separations, the dipole moment

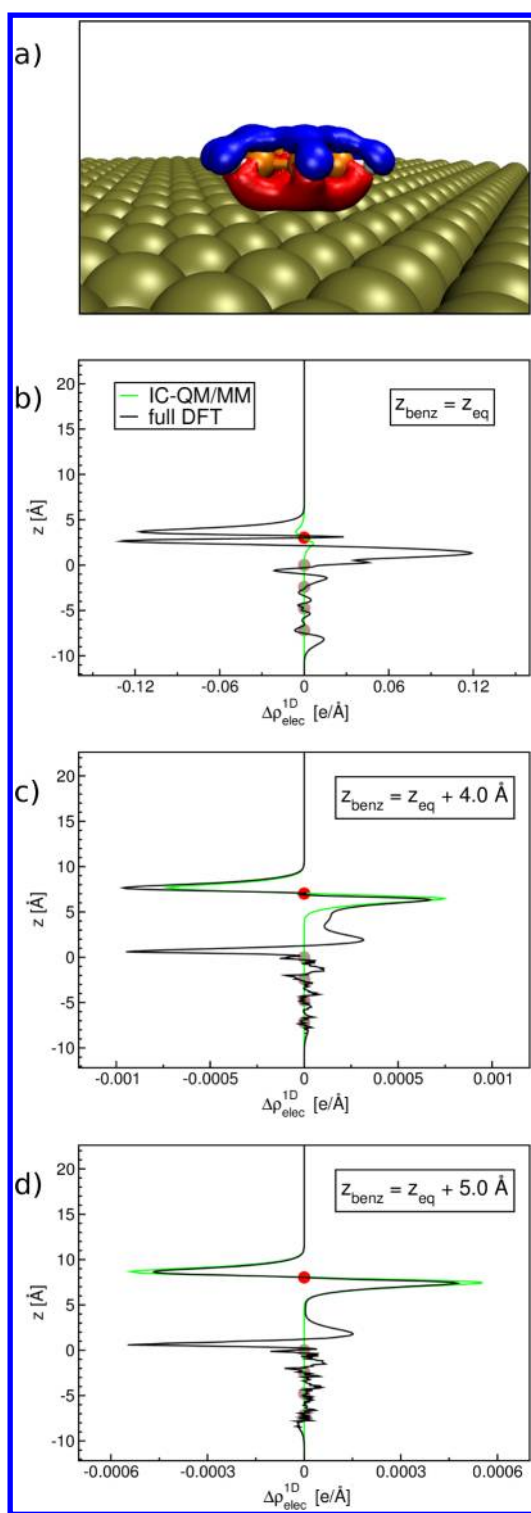


Figure 7. Difference in electron density $\Delta\rho_{\text{elec}}$ upon adsorption of benzene on Au(111). (a) Three-dimensional representation of $\Delta\rho_{\text{elec}}$ obtained with IC-QM/MM. Red regions correspond to increased and blue regions to decreased electronic density. (b–d) Plane-integrated density difference $\Delta\rho_{\text{elec}}^{1D}$. Brown spheres indicate the position of the metal layers and the red sphere the position z_{benz} of benzene. z_{eq} indicates the equilibrium separation obtained by full DFT.

converges to the value for an isolated guanine molecule or in other words, to the QM/MM value without image charges (see also SI Figure S4).

Table 2. Dipole Moments μ (Debye) for Nitrobenzene, Thymine, and Guanine Adsorbed on Au(111)^a

method	μ_x	μ_y	μ_z	$ \mu $	$\Delta \mu $
nitrobenzene					
QM/MM	−4.59	−0.29	−0.25	4.61	0.15
IC-QM/MM	−4.75	−0.30	−0.25	4.76	
thymine					
QM/MM	−4.02	−1.50	0.06	4.29	0.17
IC-QM/MM	−4.19	−1.55	0.06	4.46	
guanine					
QM/MM	6.53	−0.97	0.35	6.61	0.23
IC-QM/MM	6.75	−1.03	0.43	6.84	

^a μ_x , μ_y , and μ_z are the x -, y -, and z -component of the dipole vector respectively. IC-QM/MM structures have been used for all adsorbates.

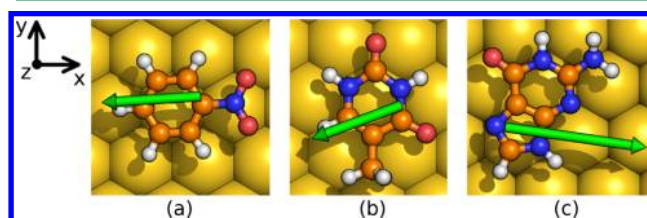


Figure 8. Dipole moments (green arrows) of the adsorbates with atomic coordinates optimized by IC-QM/MM. (a) Nitrobenzene, (b) thymine, and (c) guanine on Au(111).

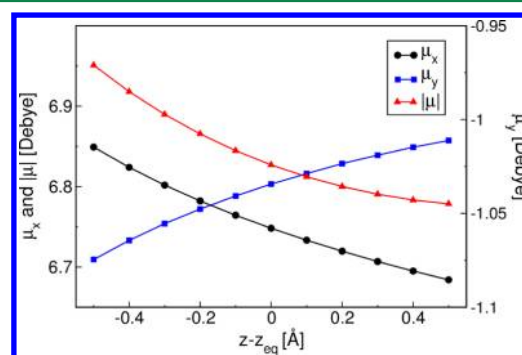


Figure 9. Variation of the dipole moment μ in Debye for guanine adsorbed on Au(111) dependent on the molecule-surface separation. μ_x and μ_y are the x - and y -component of the dipole vector, respectively. z_{eq} is the equilibrium position of the molecule as obtained from the IC-QM/MM model.

4.3. Water on Pt(111). **4.3.1. Static Calculations of Water Clusters.** Starting with the geometry of a single water molecule on Pt(111), the molecule-surface separation predicted by full DFT is with 2.38 Å considerably smaller than for aromatic adsorbates on Au(111). Hence, stronger induction effects are expected potentially causing structural changes. While the distance is essentially the same with all three models, the induced charges play an important role in determining the tilt angle. The latter is defined as the angle between surface normal and dipole vector of the H_2O molecule. According to full DFT results, the H_2O monomer binds preferentially at atop sites and lies nearly flat on the surface with a tilt angle of roughly 75°. Similar results were reported in ref 53. Atop binding is also observed with the QM/MM potential describing the interactions between water and platinum. The empirical potential was designed to rotate the molecule such that the hydrogens point up. That means, a small angle between surface normal and dipole moment is energetically favored. The angle

predicted by full DFT is roughly 60° larger indicating an attractive interaction between hydrogens and platinum. IC-QM/MM yields an angle that is approximately 10° closer to full DFT. Despite the fact, that the difference to full DFT is still large, image charges account at least partly for the rotation of the tilt angle. This demonstrates that polarization effects are important for modeling the interactions between hydrogen and platinum. Structural differences become much more pronounced when several water molecules are adsorbed on Pt(111). The changes in geometry compared to QM/MM without image charges are reported in Figure 10. The most

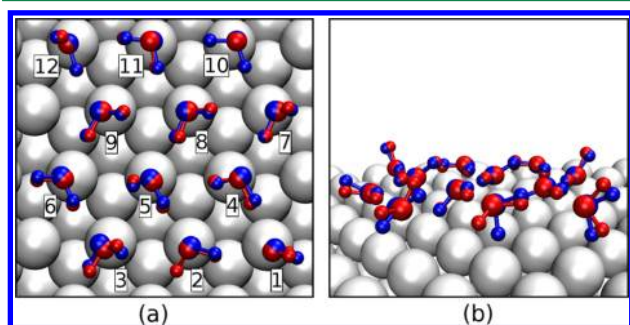


Figure 10. Top view (a) and perspective (b) view of the optimized structures of the $12\text{H}_2\text{O}$ water adsorbed on Pt(111). Red: structure optimization using QM/MM without IC. Blue: structure optimization using IC-QM/MM.

remarkable effect of the image charges is that water is not only adsorbed via metal–oxygen (M–O) but also via metal–hydrogen (M–HO) bonds. “H-down” water molecules are also predicted by full DFT structure optimization. Experimental studies^{54–56} using X-ray absorption, X-ray emission and X-ray photoelectron spectroscopy found, indeed, that water is adsorbed (intact) with both Pt–O and Pt–HO bonding species on Pt(111). More recent studies of water monolayers on Pt(111) employing scanning tunneling⁵⁷ and vibrational spectroscopy⁵⁸ found a so-called $\sqrt{39}$ structure of the monolayer. Nonbonded hydrogens in this structure show also the preference to point toward the surface rather than away.

The interaction and adsorption energies of the water clusters are reported in Table 3. The contribution of the image charges to the interaction energies is roughly -3 kJ/mol for H_2O and $2\text{H}_2\text{O}$, which agrees with the values reported in ref 15. For $12\text{H}_2\text{O}$, the contribution of the image charges is two times larger indicating that the overall polarization effect is increased with increasing number of adsorbates. Generally, the IC-QM/MM energies are close to the energies predicted by full DFT. Especially, the adsorption energies obtained with IC-QM/MM show good agreement with the full DFT results. The deviation is less than 4.0 kJ/mol for all water systems. Comparing interaction and adsorption energies, it is to note that the latter

contain also intermolecular hydrogen bonding $E_{\text{H-bond}}$ resulting in more negative values for the adsorption energies of the clusters.

The increase in dipole moment is almost marginal for a single molecule upon introduction of polarization. However, the changes in electronic structure are much more pronounced for a whole water cluster. Table 4 summarizes the results for

Table 4. Dipole Moments μ in Debye for $12\text{H}_2\text{O}$ on Pt(111)^a

molecule no.	$ \mu _{\text{IC-QM/MM}}$	IC-QM/MM structure		QM/MM structure	
		$ \mu _{\text{QM/MM}}$	$\Delta \mu $	$ \mu _{\text{QM/MM}}$	$\Delta \mu $
1	2.52	2.44	0.08	2.47	0.05
2	2.64	2.49	0.15	2.49	0.15
3	2.45	2.38	0.07	2.14	0.31
4	2.71	2.55	0.16	2.48	0.23
5	2.67	2.53	0.14	2.52	0.15
6	2.54	2.46	0.08	2.40	0.14
7	2.42	2.29	0.13	2.18	0.24
8	2.52	2.39	0.13	2.34	0.18
9	2.75	2.64	0.11	2.53	0.22
10	2.01	1.98	0.03	1.97	0.04
11	2.30	2.26	0.04	2.25	0.05
12	2.25	2.17	0.08	2.17	0.08

^a $\Delta|\mu|$ is the deviation of the dipole moments comparing IC-QM/MM and QM/MM. The molecule numbers correspond to the numbering in Figure 10(a).

$12\text{H}_2\text{O}$. The dipole moments obtained with QM/MM and IC-QM/MM have been calculated for the respective structures presented in Figure 10. The numbering of the molecules corresponds to the one shown in Figure 10(a). The dipole moment of a single water molecule in the cluster can be up to 0.7 D larger than in gas phase (1.85 D⁵⁹) due to the formation of hydrogen bonds (H-bonds) with neighboring water molecules. Significantly larger dipole moments are already obtained by the QM/MM description omitting polarization. Several theoretical^{60,61} studies have already exhaustively discussed this phenomenon. For reference, DFT simulations with the PBE functional predict average dipole moments of bulk water between 3.10 to 3.27 D.^{60,62,63} In addition to that, the effect of the IC polarization induces a further enhancement of the molecular dipoles up to 0.3 D. In particular, molecule 3 undergoes the largest dipole-change. Namely, by introducing the IC polarization, molecule 3 changes its orientation and moves toward molecule 6 (see Figure 10(a)), strengthening the corresponding H-bond. In general, the changes in dipole moments are due to both, the structural changes and the difference in the electrostatic potential given by the image charges.

Table 3. Interaction E_{int} (kJ/mol) and Adsorption Energies E_{ads} (kJ/mol) of Water Clusters on Pt(111)^a

	H_2O		$2\text{H}_2\text{O}$			$12\text{H}_2\text{O}$		
	E_{int}	E_{ads}	E_{int}	E_{ads}	$E_{\text{H-bond}}$	E_{int}	E_{ads}	$E_{\text{H-bond}}$
QM/MM	−41.6	−37.3	−40.9	−49.2	−10.6	−36.4	−61.9	−26.0
IC-QM/MM	−44.2	−43.6	−43.7	−52.9	−10.5	−42.8	−66.6	−24.4
full DFT	−44.9	−43.5	−50.6	−56.8	−7.0	−44.2	−63.0	−19.7

^a E_{ads} includes intermolecular hydrogen bonding $E_{\text{H-bond}}$ (kJ/mol per molecule). Energies are given for the structure optimized with the respective method.

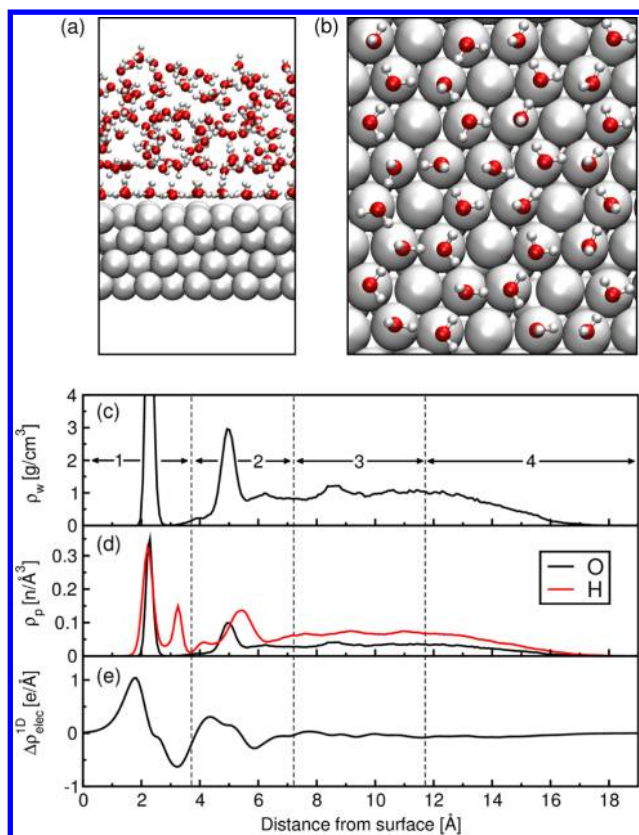


Figure 11. Structural and electronic properties obtained for a water film on Pt(111). (a) Typical snapshot of the water/Pt(111) simulation cell. (b) Snapshot of the water adlayer. (c) Plane-averaged water density ρ_w along the surface normal. The arrows indicate the division of the water film in four different layers. (d) Plane-averaged particle density ρ_p for O and H atoms. (e) Plane-integrated electronic density difference $\Delta\rho_{\text{elec}}^{\text{ID}}$ between water and Pt(111).

4.3.2. MD Simulation of a Water Film. A typical snapshot of the water film on Pt(111) and the first adsorbed water layer (adlayer) are presented in Figure 11(a and b). The water molecules of the adlayer form hexagonal rings, which are experimentally and theoretically observed for water adsorbed at (111) surfaces of several fcc metals.^{56,64,65} The vacancies in the honeycomb-like structure are locally occupied resulting in an average coverage of 70% of all top sites.

The plane-averaged density of the water molecules as function of the distance from the surface is displayed in Figure 11(c). The sharp peak at 2.36 Å indicates the adlayer followed by a ~ 3 Å thick region of density depletion. A second peak is found at about 5 Å showing that the metallic substrate also dictates the water structure in the second adsorption layer. Compared to bulk water, the water molecules in these regions are expected to be massively overstructured. Further away from the surface, the density oscillations decay rapidly. For distances larger than 10 Å, the density corresponds to the one of bulk water. At the liquid–vacuum interface, the density finally decreases to zero.

For further discussion of structural and electronic properties, the water film was split in four separate layers guided by the oscillations in the density profile, see Figure 11(c). Radial distribution functions (RDFs) for each layer are reported for oxygen–oxygen (O–O) and oxygen–hydrogen (O–H) in Figure 12(a and b). The curves for the second and third layer resemble RDFs of bulk liquid water obtained with DFT-PBE in

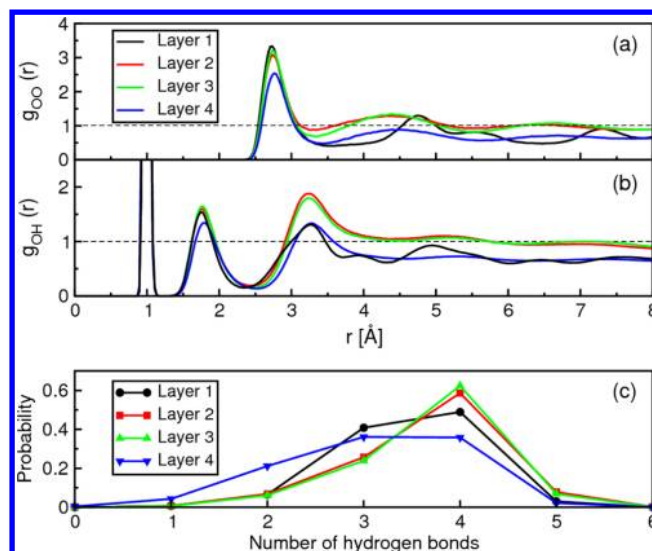


Figure 12. Structural properties for the four different layers of the water film defined in Figure 11(c). (a) Oxygen–oxygen and (b) oxygen–hydrogen RDFs. (c) Distribution of the total number of H-bonds per molecule.

previous studies.^{60,66} The peaks for the water–metal and water–vacuum layers are located at the same distance. However, the peak heights of the fourth layer are significantly smaller due to the reduced coordination at the water–vacuum interface. Even though the coordination is also reduced for the adlayer along the z -axis, the peak heights at 2.7 Å (O–O) and 1.7 Å (O–H) are comparable to bulk water. For larger distances, the RDFs decay to values smaller than 1 and show several additional peaks. This is in agreement with the plane-averaged density profile predicting an overstructuring in the adlayer, which compensates the lacking coordination in the third dimension for small, but not for large distances.

First insights in the nature of hydrogen bonding at the metallic interface are given by the plane-averaged distributions of O and H atoms, see Figure 11(d). The onset of the hydrogen distribution is at shorter distances thanks to the reorientation induced by the polarization of the image charges, that is, some H atoms are pointing toward the substrate, which was already observed for the water clusters. The largest fraction of the hydrogens of the adlayer are located in the plane of the oxygen atoms indicated by the large peak at 2.36 Å. The small H atom peak at 3.2 Å, located in the region of density depletion, implies that a fraction of the water molecules in the adlayer forms H-bonds with the acceptors of the second layer. This is confirmed by more detailed analysis using a standard criterion for defining an H-bond.^{67,68} Almost half of the water molecules of the adlayer donate one of their H atoms to the bulk. The second H atom functions as H-bond donor in the plane of the adlayer. For further investigation of the H-bond network, the average number of H-bonds for each molecule (accepted and donated) was calculated and the distribution for each layer has been plotted in Figure 12(c). From the results, we can see that most of the molecules of the second and third layer have four H-bonds. At the liquid/metal interface, the probability of the formation of four H-bonds is significantly reduced, while the probability of forming only three H-bonds increases. From that, we can conclude that the geometry of the metal surface dictates hydrogen bonding patterns that are incommensurate with the tetrahedral structure characteristic for bulk water. This leads to

unfavorable interactions with the adjacent liquid resulting in a region of density depletion.

Simulations of a similar system within a purely classical frame using the same empirical interaction potential and a classical version of the IC approach are reported in ref 16. We obtain very similar results for the profile of the water density and the structure of the adlayer. However, in the purely classical model, more vacancies are occupied resulting in a 15% larger coverage. The average density of hydrogens donated to the bulk is approximately five times larger with our method. This suggests that in our IC-QM/MM description the adlayer is less hydrophobic than predicted by the purely classical model. The latter implies that the interactions between the water molecules predicted by the DFT-PBE potential are stronger than for the classical potential (SPC/E), which is confirmed by structural and dynamical properties such as RDFs or diffusion coefficients^{66,69,70} and thermodynamic properties.⁷¹

Comparing the structural properties of the water/metal interface predicted by IC-QM/MM to experiments and *ab initio* calculations, we find that our model reproduces some crucial features of the $\sqrt{39}$ structure. The water molecules form H-bonds predominately in the plane of the adlayer and nonbonded hydrogens point down to the surface. Hexagonal rearrangements are also structural motives occurring in the $\sqrt{39}$ structure. However, the formation of five- and seven-membered rings is not captured.

IC-QM/MM allows also some insight in the electronic rearrangements upon adsorption of the water film. The plane-integrated electronic density difference is displayed in Figure 11(e). Electron accumulation is observed below and depletion above the adlayer. Compared to the adsorption of a single nonpolar molecule such as benzene, the polarization is orders of magnitude larger. The electronic polarization extends also into the second layer, but decreases to zero in the third layer. The average dipole moment in the bulk-like layers is ~ 3.0 D and about 0.2 D smaller at the liquid/vacuum interface due to a reduced number of H-bonds. Even though the latter is true at the metal/liquid interface, the average dipole moment is also 3.0 D, which must be attributed to polarization effects.

The observed structural and electronic properties are strongly affected by the presence of the IC interactions with the QM molecules. This is easily verified by switching off these interactions and following the MD trajectory as generated by the bare QM/MM scheme. As a result, the first layer of water molecules in contact with the Pt surface is destabilized. The ordered arrangement is disrupted in a few ps and some molecules dissociate. This unphysical phenomenon is most probably a consequence of the strong distortion forces arising by suddenly switching off the image charges. As shown in SI Figure S5, the IC contributions significantly change the electrostatic potential over a range of more than 10 Å above the surface.

5. CONCLUSIONS

In this work, an image charge augmented QM/MM method has been introduced to enable QM/MM simulations of molecules adsorbed on metallic surfaces. With IC-QM/MM, important polarization effects are included explicitly. The method has been evaluated using a few simple test systems such as benzene, nitrobenzene, thymine, and guanine on Au(111). It has been demonstrated that our model reproduces the essential physics; that is, the potential within the metal is screened and the

induced charges display the expected distribution in the substrate layers. We could show that the IC-QM/MM method substantially strengthens the interaction between molecules and metal and can reproduce at least partially the electrostatic response of the molecular charge density to the induced charges. Close to the surface, the rearrangement of the electronic structure is not sufficiently captured by a pure polarization model since the molecular and metallic charge densities are not separated. However, IC-QM/MM is expected to model the long-range interactions correctly.

Our method has been further evaluated with small water clusters adsorbed at Pt(111). Interaction and adsorption energies agree well with full DFT results set as benchmark. Pronounced structural changes attributed to polarization effects are observed for the largest cluster. By comparing to experimental data, we could show that the IC-QM/MM structure is reasonable.

We applied our method to perform an MD simulation of a liquid water/Pt(111) interface. Structural analysis of the water film and especially the adlayer, reveals that the water molecules bind strongly to the surface and that the hydrogen bonding is frustrated by the geometry of the surface. The water–metal interface is thus hydrophobic, but more hydrophilic than predicted by purely classical simulations. As discussed in ref 16, the reorganization in the adlayer occurs at time scales larger than nanoseconds. Obtaining dynamical properties at these time scales with *ab initio* MD is out of scope but possible to address with the IC-QM/MM approach. IC-QM/MM is potentially a valuable tool to study these interfaces with large-scale MD and to allow implications on electrochemical properties of metal electrodes. Successful application of the classical equivalent of the IC approach in electrochemistry^{18–20} also suggests that the method holds promise especially for electrochemical systems.

■ ASSOCIATED CONTENT

Supporting Information

Contour plot of the electrostatic potential for nitrobenzene on Au(111), charges induced in finite Au(111) slabs by Cl^- and Na^+ , $\Delta\rho_{\text{elec}}$ for benzene on Au(111) as obtained by full DFT, variation of the dipole moment (x -, y -, and z -component) for guanine on Au(111), plane-averaged electrostatic potential of 151 H_2O on Pt(111) for a particular snapshot of the MD simulation. This material is available free of charge via the Internet at <http://pubs.acs.org/>.

■ AUTHOR INFORMATION

Corresponding Authors

*E-mail: d.golze@pci.uzh.ch.

*E-mail: m.iannuzzi@pci.uzh.ch.

*E-mail: hutter@pci.uzh.ch.

Notes

The authors declare no competing financial interest.

■ ACKNOWLEDGMENTS

We thank the Swiss National Supercomputing Centre (CSCS) for providing computational resources and Dr. Ari P. Seitsonen for fruitful discussions.

■ REFERENCES

- (1) Warshel, A.; Levitt, M. J. *Mol. Biol.* **1976**, *103*, 227–249.

- (2) Taddei, M. M.; Mendes, T. N. C.; Farina, C. *Eur. J. Phys.* **2009**, *30*, 965–972.
- (3) Griffiths, D. J. *Introduction to Electrodynamics*, 3rd ed.; Pearson Education: San Francisco, CA, 2008; pp 121–126.
- (4) Tomba, G.; Stengel, M.; Schneider, W.-D.; Baldereschi, A.; Vita, A. D. *ACS Nano* **2010**, *4*, 7545–7551.
- (5) Yokoyama, T.; Takahashi, T.; Shinozaki, K.; Okamoto, M. *Phys. Rev. Lett.* **2007**, *98*, 206102.
- (6) Wernersson, E.; Kjellander, R. *J. Chem. Phys.* **2006**, *125*, 154702.
- (7) Kantorovich, L. N.; Livshits, A. I.; Stoneham, M. J. *Phys.: Condens. Matter* **2000**, *12*, 795–814.
- (8) Bocquet, F.; Nony, L.; Loppacher, C. *Phys. Rev. B* **2011**, *83*, 035411.
- (9) Sadeghi, A.; Baratoff, A.; Ghasemi, S. A.; Goedecker, S.; Glatzel, T.; Kawai, S.; Meyer, E. *Phys. Rev. B* **2012**, *86*, 075407.
- (10) Finnis, M. W. *Surf. Sci.* **1991**, *241*, 61–72.
- (11) Finnis, M. W.; Kaschner, R.; Kruse, C.; Furthmüller, J.; Scheffler, M. *J. Phys.: Condens. Matter* **1995**, *7*, 2001–2019.
- (12) Tarmyshov, K. B.; Müller-Plathe, F. *J. Chem. Phys.* **2007**, *126*, 074702.
- (13) Iori, F.; Corni, S. *J. Comput. Chem.* **2008**, *29*, 1656–1666.
- (14) Iori, F.; Felice, R. D.; Molinari, E.; Corni, S. *J. Comput. Chem.* **2009**, *30*, 1465–1476.
- (15) Siepmann, J. I.; Sprik, M. *J. Chem. Phys.* **1995**, *102*, 511–524.
- (16) Limmer, D. T.; Willard, A. P.; Madden, P.; Chandler, D. *Proc. Natl. Acad. Sci. U.S.A.* **2013**, *110*, 4200–4205.
- (17) Willard, A. P.; Reed, S. K.; Madden, P. A.; Chandler, D. *Faraday Discuss.* **2009**, *141*, 423–441.
- (18) Reed, S. K.; Lanning, O. J.; Madden, P. A. *J. Chem. Phys.* **2007**, *126*, 084704.
- (19) Merlet, C.; Rotenberg, B.; Madden, P. A.; Taberna, P.-L.; Simon, P.; Gogotsi, Y.; Salanne, M. *Nat. Mater.* **2012**, *11*, 306–310.
- (20) Vatamanu, J.; Cao, L.; Borodin, O.; Bedrov, D.; Smith, G. D. *J. Phys. Chem. Lett.* **2011**, *2*, 2267–2272.
- (21) Senn, H. M.; Thiel, W. *Angew. Chem., Int. Ed.* **2009**, *48*, 1198–1229.
- (22) Guallar, V.; Wallrapp, F. H. *Biophys. Chem.* **2010**, *149*, 1–11.
- (23) Hu, H.; Yang, W. *Annu. Rev. Phys. Chem.* **2008**, *59*, 573–601.
- (24) Senn, H. M.; Thiel, W. *Curr. Opin. Chem. Biol.* **2007**, *11*, 182–187.
- (25) Friesner, R. A.; Guallar, V. *Annu. Rev. Phys. Chem.* **2005**, *56*, 389–427.
- (26) Fischer, D.; Curioni, A.; Andreoni, W. *Langmuir* **2003**, *19*, 3567–3571.
- (27) Sushko, M. L.; Sushko, P. V.; Abarenkov, I. V.; Shluger, A. L. *J. Comput. Chem.* **2010**, *31*, 2955–2966.
- (28) Illingworth, C. J. R.; Gooding, S. R.; Winn, P. J.; Jones, G. A.; Ferenczy, G. G.; Reynolds, C. A. *J. Phys. Chem. A* **2006**, *110*, 6487–6497.
- (29) Houjou, H.; Inoue, Y.; Sakurai, M. *J. Phys. Chem. B* **2001**, *105*, 867–879.
- (30) Thompson, M. A.; Schenter, G. K. *J. Phys. Chem.* **1995**, *99*, 6374–6386.
- (31) Lippert, G.; Hutter, J.; Parrinello, M. *Mol. Phys.* **1997**, *92*, 477–488.
- (32) Laino, T.; Mohamed, F.; Laio, A.; Parrinello, M. *J. Chem. Theory Comput.* **2005**, *1*, 1176–1184.
- (33) Laino, T.; Mohamed, F.; Laio, A.; Parrinello, M. *J. Chem. Theory Comput.* **2006**, *2*, 1370–1378.
- (34) The CP2K developers group, CP2K is freely available from <http://www.cp2k.org/> (accessed April 3, 2013).
- (35) VandeVondele, J.; Krack, M.; Mohamed, F.; Parrinello, M.; Chassaing, T.; Hutter, J. *Comput. Phys. Commun.* **2005**, *167*, 103–128.
- (36) VandeVondele, J.; Hutter, J. *J. Chem. Phys.* **2007**, *127*, 114105.
- (37) Goedecker, S.; Teter, M.; Hutter, J. *Phys. Rev. B* **1996**, *54*, 1703–1710.
- (38) Hartwigsen, C.; Goedecker, S.; Hutter, J. *Phys. Rev. B* **1998**, *58*, 3641–3662.
- (39) Krack, M. *Theor. Chem. Acc.* **2005**, *114*, 145–152.
- (40) Perdew, J. P.; Burke, K.; Ernzerhof, M. *Phys. Rev. Lett.* **1996**, *77*, 3865–3868.
- (41) Grimme, S.; Antony, J.; Ehrlich, S.; Krieg, H. *J. Chem. Phys.* **2010**, *132*, 154104.
- (42) Foiles, S. M.; Baskes, M. L.; Daw, M. S. *Phys. Rev. B* **1986**, *33*, 7983–7991.
- (43) LAMMPS, Large-scale Atomic/Molecular Massively Parallel Simulator, <http://lammps.sandia.gov/> (accessed April 22, 2012).
- (44) Rapino, S.; Zerbetto, F. *Langmuir* **2005**, *21*, 2512–2518.
- (45) Grimme, S. *J. Comput. Chem.* **2006**, *27*, 1787–1799.
- (46) Boys, S. F.; Bernardi, F. *Mol. Phys.* **1970**, *19*, 553–566.
- (47) van Duijneveldt, F. B.; van Duijneveldt-van de Rijdt, J. G. C. M.; van Lenthe, J. H. *Chem. Rev.* **1994**, *94*, 1873–1885.
- (48) Wannier, G. H. *Phys. Rev.* **1937**, *52*, 191–197.
- (49) Marzari, N.; Vanderbilt, D. *Phys. Rev. B* **1997**, *56*, 12847–12865.
- (50) Chwee, T. S.; Sullivan, M. B. *J. Chem. Phys.* **2012**, *137*, 134703.
- (51) Bader, R. F. W. *Atoms in Molecules: A Quantum Theory*; Clarendon Press: Oxford, 1990; pp 248–351.
- (52) Tang, W.; Sanville, E.; Henkelman, G. *J. Phys.: Condens. Matter* **2009**, *21*, 084204.
- (53) Michaelides, A.; Ranea, V. A.; de Andres, P. L.; King, D. A. *Phys. Rev. Lett.* **2003**, *90*, 216102.
- (54) Ogasawara, H.; Brena, B.; Nordlund, D.; Nyberg, M.; Pelmenchikov, A.; Pettersson, L. G. M.; Nilsson, A. *Phys. Rev. Lett.* **2002**, *89*, 276102.
- (55) Hodgson, A.; Haq, S. *Surf. Sci. Rep.* **2009**, *64*, 381–451.
- (56) Schiros, T.; Andersson, K. J.; Pettersson, L. G. M.; Nilsson, A.; Ogasawara, H. *J. Electron Spectrosc. Relat. Phenom.* **2010**, *177*, 85–98.
- (57) Nie, S.; Feibelman, P. J.; Bartelt, N. C.; Thürmer, K. *Phys. Rev. Lett.* **2010**, *105*, 026102.
- (58) Feibelman, P. J.; Kimmel, G. A.; Smith, R. S.; Petrik, N. G.; Zubkov, T.; Kay, B. D. *J. Chem. Phys.* **2011**, *134*, 204702.
- (59) McLeary, K. S. In *Water Encyclopedia. Physical Properties*; Lehr, J. H., Keeley, J., Eds.; John Wiley & Sons, Inc.: New York, 2005.
- (60) Liu, L.-M.; Krack, M.; Michaelides, A. *J. Chem. Phys.* **2009**, *130*, 234702.
- (61) McGrath, M. J.; Siepmann, J. I.; Kuo, I.-F. W.; Mundy, C. J. *Mol. Phys.* **2007**, *105*, 1411–1417.
- (62) Cicero, G.; Grossman, J. C.; Schwegler, E.; Gygi, F.; Galli, G. *J. Am. Chem. Soc.* **2008**, *130*, 1871–1878.
- (63) Todorova, T.; Seitsonen, A. P.; Hutter, J.; Kuo, I.-F. W.; Mundy, C. J. *J. Phys. Chem. B* **2006**, *110*, 3685–3691.
- (64) Tatarikhanov, M.; Ogletree, D. F.; Rose, F.; Mitsui, T.; Fomin, E.; Maier, S.; Rose, M.; Cerdá, J. I.; Salmeron, M. *J. Am. Chem. Soc.* **2009**, *131*, 18425–18434.
- (65) Michaelides, A.; Morgenstern, K. *Nat. Mater.* **2007**, *6*, 597–601.
- (66) Lin, I.-C.; Seitsonen, A. P.; Tavernelli, I.; Rothlisberger, U. *J. Chem. Theory Comput.* **2012**, *8*, 3902–3910.
- (67) Luzar, A.; Chandler, D. *Phys. Rev. Lett.* **1996**, *76*, 928–931.
- (68) Luzar, A.; Chandler, D. *Nature* **1996**, *379*, 55–57.
- (69) Mark, P.; Nilsson, L. *J. Phys. Chem. A* **2001**, *105*, 9954–9960.
- (70) Chatterjee, S.; Debenedetti, P. G.; Stillinger, F. H.; Lynden-Bell, R. M. *J. Chem. Phys.* **2008**, *128*, 124511.
- (71) McGrath, M. J.; Siepmann, J. I.; Kuo, I.-F. W.; Mundy, C. J. *Mol. Phys.* **2006**, *104*, 3619–3626.